# A numerical model for predicting the aerodynamic characteristics of propelling nozzles

**Aws Al-Akam**
**alakam.aws@gmail.com**
Former PhD student at Propulsion Engineering Centre, School of Aerospace, Transport, and Manufacturing, Cranfield University
Babylon University, College of Engineering
Hilla, Babil
Iraq

**Theoklis Nikolaidis, David G. MacManus, Ioannis Goulos**
Cranfield University
Propulsion Engineering Centre, School of Aerospace, Transport, and Manufacturing
MK43 0AL
Bedfordshire
England

## ABSTRACT

It is essential to predict the exhaust-system performance of the aero-engine during the design stages as it plays a critical role in the engine components matching. In addition to this, it has an impact on the overall engine performance. Consequently, it is important to model the complex flow features around the exhaust system accurately in order to capture the flow characteristics. Computational Fluid Dynamics (CFD) alongside with low-order models can play a central role in the design and performance assessment of the propulsion system. This paper aims to explore the suitability of a numerical model, boundary conditions, and the employed mesh topology in computing a propelling

nozzle performance. The current work is a first step towards building a module to assess a wide range of nozzle configurations at the preliminary design stages.

A single-stream and plug-nozzle propelling nozzle were simulated for this purpose. For the single-stream nozzle, the simulations were run at various flight conditions and different geometrical features. For both nozzle configurations, a comparison between the effectiveness of six turbulence models to capture the nozzle flow features is presented. The validated module is then used to assess the impact of the bypass flow and the plug half-angle on the performance of the core nozzle for a dual-stream nozzle configuration. The calculated nozzle efficiencies are lower than the experimental data for both nozzle types, with a maximum difference of single-stream nozzle efficiency ≈ -3.29% at NPR = 1.83 and by -0.84% at NPR = 3.88 and for the plug nozzle with -1.05% at NPR 2.64 and across a range from -0.46% to -0.68% between NPR = 3.14 to 5.3. The application of RANS k-ω SST turbulence model showed the best results as compared with the standard k-ε, RNG k-ε, realizable k-ε, and Spalart-Allmaras models in simulating the propelling nozzles aerodynamics. Generally, the results show the strength and the weakness of the numerical module in simulating the nozzle flow features and predicting its performance. Moreover, the Fan Nozzle Pressure Ratio (FNPR) and the plug half-angle (ω) has a noticeable impact on the overall and core nozzle performance. Moreover, the combined impact of both parameters has a noticeable impact on the propelling nozzle performance.

**Keywords:** Propelling nozzle, nozzle aerodynamics, thrust coefficient, plug nozzle.

# NOMENCLATURE

| | |
|---|---|
| $A_e$ | Nozzle exit area [m$^2$] |
| $A_{in}$ | Nozzle inlet area [m$^2$] |
| $C_{D\beta}$ | Pressure drag coefficient |
| *CFD* | computational fluid dynamics |
| *Cp* | pressure coefficient $= \frac{p-p_\infty}{0.5\rho V_\infty^2}$ |
| Cv | Velocity coefficient [-] |
| Cd | Discharge coefficient [-] |
| $D_{max}$ | Maximum diameter, [m] |
| *D* | Pressure Drag,[N] |
| *F* | Gross thrust, [N] |
| *GCI* | grid convergence index |
| $l_{bt}$ | Boat-tail length, [m] |
| $l_{pl}$ | Plug length,[m] |
| $l_{sc}$ | Shock cell length,[-] |
| $l_{us}$ | Upstream distance from the CFD inlet plane [m] |
| $\dot{m}$ | Mass Flow rate,[kg/s] |
| $M_\infty$ | Mach number |
| *NPR* | nozzle pressure ratio |
| *p* | Local static pressure, [pa] |
| *P7* | Total pressure at the nozzle inlet, [pa] |
| $T_{tin}$ | Total temperature at the nozzle inlet, [K] |
| *TR* | Ratio of the total temperature at the nozzle inlet to the free-stream static temperature [-] |
| $\beta_c$ | Boat-tail Chord angle, [°] |
| ω | Plug-half angle, [°] |
| θ | Boundary-layer momentum thickness [m] |
| Φ | Forces component [N] |
| $\Delta Cp$ | pressure coefficient difference,[-] $=CP_{exp} - CP_{CFD}$ |
| $\Delta Cp_{ave}$ | Absolute average pressure coefficient difference,[-] |
| $\Delta \frac{p}{P_7}$ | Pressure ratio difference,[-] |
| $V_e$ | Exit velocity,[m/s] |

## 1.0 INTRODUCTION

The propelling nozzle of the aero-engine generates the engine thrust. The losses through the exhaust system can significantly affect the overall performance of the engine. Moreover, the geometrical and the operational parameters variation could affect the nozzle characteristics. Therefore, the nozzle performance should be assessed correctly in the early design phases. Recently, computational methods play a crucial role in preliminary design stages to evaluate nozzle's performance.

Parametric studies can be conducted on the nozzle geometry to assess the impact of the geometrical features on the nozzle performance [1]. Lennard et al. [1] showed that the change in the by-pass and the core nozzle geometrical profile increases the thrust coefficient for an engine running at the cruise conditions (high nozzle pressure ratio)

and reduces the discharge coefficient. The thrust coefficient of the new configuration improved by 0.4% as compared with the conventional at the fan nozzle pressure ratio (NPR) of 2.74. Zimmermann et al. [2] studied the effect of changing the length of the core-cowl of an ultra-high bypass ratio turbofan, as well as evaluated the impact of the change in the static back pressure and its impact on the nozzle discharge coefficient by using a RANS method coupled with the standard k-ε model. The results showed that as the core-cowl length increases, there is a reduction in the fan nozzle discharge coefficient and an increase in the thrust coefficient by 0.4% and 1.2%, respectively. However, the core nozzle showed an increase in the flow coefficient by 10% and a reduction in the thrust coefficient by 4.3%. Moreover, Zhang et al. [3], Spotts et al. [4] and Dippold et al. [5] reported the was an impact on the discharge and thrust coefficient when the half-angle of the nozzle internal walls was varied. Furthermore, at cruise conditions, Lahti et al., [6] indicated that the thrust coefficient influenced noticeably by changing the throat inner wall curvature. This was also pointed out by Malecki and Lord [7], they showed that the different radius of curvature of the fan nozzle the nozzle efficiency increased by 1.0% at nozzle pressure ratio (NPR) of 1.6 and 2.1. Zimmermann et al., [2,8] showed that the discharge coefficient of the fan nozzle and an increase in the thrust coefficient by 0.4% and 1.2%, respectively, as the length of the core-cowl was increased. Characteristic maps the nozzle were produced by Al-Akam et al., [9]as a function of the throat area and the plug nozzle for a propelling. The maps showed there is a noticeable effect of these parameters in addition to the nozzle pressure ration on the overall performance of the nozzle.

In any case, the results of these methods should compare the experimental data, by means of performing a validation task. Peery and Forester [10] conducted a validation study on a single stream, plug and multi-stream nozzle configuration, for a numerical method using two-dimensional Navier-stokes equation. A wall function was used to capture the viscous flow over the nozzle solid surfaces. Three different eddy viscosity models were used to calculate the turbulent viscosity. The pressure distribution over the cowl after-body surfaces for the multi-stream nozzle showed an agreement with the experimental data with a percentage pressure difference of -0.3% at the nozzle edge. However, an under-prediction of the shock waves strength was observed over the core-cowl surface and an over-prediction over the plug surface. Zhang Y et al.,[11] used the NSAWET code to simulate a conical single stream nozzle. The utilised numerical model is based on the finite volume discretisation method, using a third-order MUSCL scheme coupled with a k-ω shear stress transport (SST) turbulence model. The results showed that the calculated results agreed with the experimental data within -0.2% to -0.5% for $C_d$ and $C_v$. Hebert and Ponsonby [12] pointed out that a computational fluid dynamics (CFD) study for the exhaust nozzle at cruise and descent phase of a civil aero-engine, are compared with the experimental with +0.15% difference of the velocity coefficient. Malecki and Lord[13] used a numerical method to analyse the performance of three different nozzle configurations (single stream, plug and dual-stream nozzle). The single-stream and the plug nozzle experimental data were extracted from Harrington [14]. The CFD calculations used a RANS method with a pressure-based solver and a standard k-ε model. The single-stream results showed an over-prediction for the nozzle velocity coefficient that is calculated at static free stream conditions and free-stream Mach number of 0.9 by a range of 1.0% and 0.2%, respectively. For the plug nozzle, the results showed a -1.2% difference from the measured data for the static condition case and -1.0% for the wind on the case. The nozzle efficiency agreement is within 0.2% with the experimental data for the dual-stream nozzle calculations. Spotts et al.,[15] and Dippold [5] examined the performance of the single stream conical nozzle using the CFD model. The calculations aimed to validate the CFD codes during the change in the nozzle internal walls angle on the performance of the nozzle. Spotts used the RANS equation in a density-based solver and three turbulence models: realisable k-ε, Menter shear stress transport and realizable q-L model. The validation results showed that the method over-predicted the discharge and the thrust coefficients. Dippold [5] used a second-order Roe numerical scheme and the k-ω SST turbulence model in the investigation of the nozzle performance for the steady state. The results showed that the numerical calculations over-predicted the thrust coefficient by 0.25% to 1.0%. Spotts et al.,[15] and Dippold [5] performed the simulations at quiescent air

conditions ($M_\infty$= 0.0) within a range of NPR from 1.4 to 7.0. One of the most recent experimental activity in the evaluation of propelling nozzle performance was presented by Mikkelsen [16]. The experimental work has been conducted on a Dual Separate Flow Reference (DSFR) nozzle. The computations were performed to validate the ability of the numerical model in predicting the nozzle performance compared with the experimental data. A pressure-based solver, coupled with realizable k-ε turbulence was used for the 3D calculations. The CFD domain was discretised using a hybrid mesh with unstructured mesh elements combined with the prismatic layer to simulate the viscous effect. The numerical calculations showed that the discharge coefficient differs from the measurements by -0.35% at high NPR and -0.67% at low NPR for the fan nozzle and with a relative difference of +0.6% for the core nozzle. Moreover, the overall thrust coefficient deviates from the experimental data by 0.03%. Abdul–Hamid [17] studied the aerodynamic characteristics of an axisymmetric CFD simulation for the turbofan (dual stream nozzle) using with a RANS method a standard k-ε turbulence model. The results showed that the mass flow rate and the thrust forces agreed with the experimental data by 0.2% and 0.6%.

Although there is a wide range of numerical studies that were performed on different propelling nozzle configurations, this work goes more insight of evaluating the impact of the nozzle geometrical features, on the nozzle aerodynamics and the numerical model performance. Furthermore, the impact of varying the free stream Mach number, which is rarely considered during the validation tasks that have been presented above has been investigated. This paper aims to explore the suitability of a numerical model, boundary conditions, and the employed mesh topology in computing propelling nozzles performance. The current work is the first step towards building a model to assess a wide range of nozzle configurations at the preliminary design stages. The flow around a single-stream [18] and plug [14] propelling nozzle were simulated for this purpose, and then the results were compared with the original experimental data regarding nozzle performance. Apart from that, this work is a first step to assess the performance of the exhaust system of an aero-engine. In which, the validated model is used to assess the impact of the core-nozzle flow interaction with the fan nozzle jet for a dual-stream nozzle configuration.

## 2.0 PAPER SCOPE

The objective of this work was to assess the ability of computational methods to capture the flow characteristics of two nozzle types (single stream and plug-nozzle). The computational results were compared with experimental data in order to validate the models. For single-stream nozzles configuration, the effect of free-stream Mach number ($M_\infty$) was investigated, across a range of $M_\infty$ = 0.4, 0.8 and 1.3 and NPR of 2.02, (Table 1). Moreover, a range of the nozzle fineness ratio ($\frac{l_{bt}}{D_{max}}$) was examined. For the plug nozzle, two free stream Mach number of $M_\infty$ = 0.6 and 0.91 and NPR of 2.66, 3.12 and 3.71 were studied, (Table 1).

Six turbulence models were examined: one–equation Spalart–Allmaras model (SA)[19], standard k-ε (sk-ε)[20], RNG k-ε, Realisable k-ε model, Standard k-ω model (sk-ω) and Shear Stress Transport model k-ω SST. The SA model is known as a one-equation model as the model includes the modelling of the turbulent viscosity only [21]. The two-equation models include the turbulence kinetic energy (k) and its dissipation rate (ε and ω). It is vital to assess the appropriate turbulence model that can predict the flow features in terms of the flow separation and the jet-spreading rate for the exhaust system of the engine. The validated model then was used to assess the impact of the fan nozzle pressure ratio (FNPR) on the performance of the core nozzle of a dual-stream nozzle configuration. The FNPR was varied across the range of 1.0, 2.0, 2.2 and 2.4. Besides that the plug half-angle (ω) was changed across a range from 10˚ to 20˚ with a step of 1.0˚, (Table 3). All the dual stream nozzle simulations were carried out at $M_\infty$ of 0.82.

**Table 1**
**CFD geometrical and operational parameters of Single stream nozzle**

| Config. No. | $(\frac{l_{bt}}{D_{max}})$ | βc (°) | NPR | $M_\infty$ | $Re_{Dmax}$ | Turbulence Models |
|---|---|---|---|---|---|---|
| **(1)** | 0.80 | 17.0 | 2.02 | 0.4, 0.8, 1.3 | $1.5x10^6$- $2.14x10^6$ | SA, sk-ε, RNG k-ε, realizable k-ε, sk-ω, SST k-ω |
| **(2)** | 1.00 | 13.7 | 2.02 | 0.4, 0.8, 1.3 | $1.5x10^6$- $2.14x10^6$ | |
| **(3)** | 1.77 | 7.9 | 2.02 | 0.4, 0.8, 1.3 | $1.5x10^6$-$2.14x10^6$ | |

**Table 2**
**CFD geometrical and operational parameters of the plug nozzle**

| | $M_\infty$ [-] | NPR [-] | Turbulence Models |
|---|---|---|---|
| **Single configuration** | 0.60 | 3.12 | SA, sk-ε, RNG k-ε, realizable k-ε, sk-ω, k-ω SST |
| | 0.91 | 2.66 | |
| | 0.91 | 3.71 | |

**Table 3**
**CFD geometrical and operational parameters of the dual-stream nozzle**

| Case# | FNPR | ω (plug-half angle) | CNPR[-] | $M_\infty$[-] |
|---|---|---|---|---|
| **1** | 1.0 | 10˚-20˚ (step 1.0˚) | 1.4-3.0 (step 0.10) | 0.82 |
| **2** | 2.0 | 10˚-20˚(step 1.0˚) | 1.4-3.0 (step 0.10) | 0.82 |
| **3** | 2.2 | 10˚-20˚(step 1.0˚) | 1.4-3.0 (step 0.10) | 0.82 |
| **4** | 2.4 | 10˚-20˚(step 1.0˚) | 1.4-3.0 (step 0.10) | 0.82 |

# 3.0 METHODOLOGY

## 3.1 Geometry Description

The single-stream nozzle configuration had a fixed closure ratio ($\frac{\text{Exit nozzle area}}{\text{Inlet nozzle area}}$) of 0.5, and variable fineness ratio ($\frac{l_{bt}}{D_{max}}$) with a range of $\frac{l_{bt}}{D_{max}}$ = 0.8, 1.0 and 1.77 as presented, (Table 1). Since the experiment has been conducted at zero angles of attack [18], axisymmetric simulations adequate for this case, ignoring the three-dimensional flow features. The geometrical characteristics were extracted from Reubush, [18], Figure 1.

A single configuration of a plug-nozzle was used for the current work simulations. The computational geometry has been designed based on the work of Harrington [14], (Figure 2). Because of the lack of information about the nozzle inlet temperature, it was decided to carry out an inlet temperature sensitivity analysis to report the effect of the temperature on the nozzle characteristics. The temperature ratio ($TR = \frac{T_{tin}}{T_\infty}$) was changed across a range from unity to 2.0. The temperature variation indicated a negligible effect on the local static pressure distribution over the plug surface. The local pressure difference is of 0.06 % at the plug leading edge, and 0.11% at the trailing edged when the TR was changed from 1.0-2.0, and the thrust coefficient decreased by 0.3%. The reason for the reduction in the thrust coefficient can be attributed to the reduction in the discharge coefficient ($C_d$) of the nozzle, in which it decreased by 0.4% as the TR doubled. This reduction in $C_d$ is due to the increase in the boundary-layer thickness over the internal walls of the nozzle with TR. The temperature ratio (TR) of unity has been chosen for the current simulations.

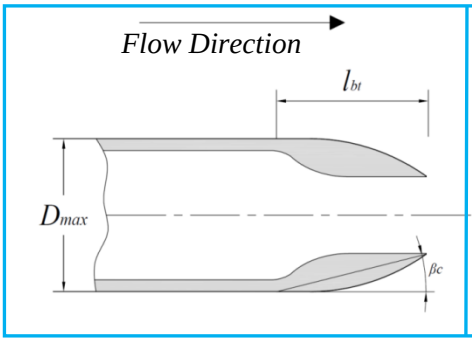


Figure 1 Schematic of the single-stream nozzle configuration.

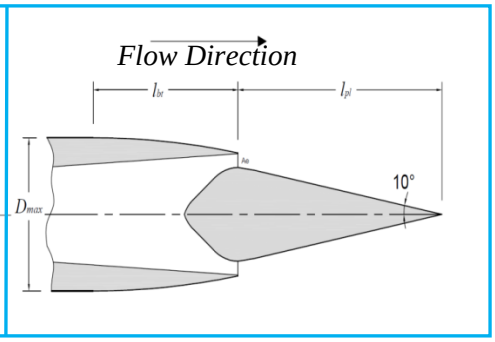


Figure 2 Schematic of the plug nozzle configuration.

Dual-stream nozzle configuration was built based on the performance data that has been extracted from an engine performance model inspired by the GE90-B85 engine class [22]**.** The performance calculations were performed at mid-cruise operating conditions (Alt.= 36000ft, $M_\infty$= 0.82), and a thrust rating of 68.24 kN. An analytical method based on Classification-Shape-Transformation (CST) was used for the parameterisation of the nozzle inner aero line to ensure smooth surface definitions. The CST method was proposed first by Kulfan and Bussoletti [23], which was derived from the basic equations that govern the aerofoil geometrical-profile. The plug was designed using a circular arc and a straight line, (Figure 3). The fan- cowl aft-body of the cowl was designed using a simple circular-arc curve, (Figure 3).

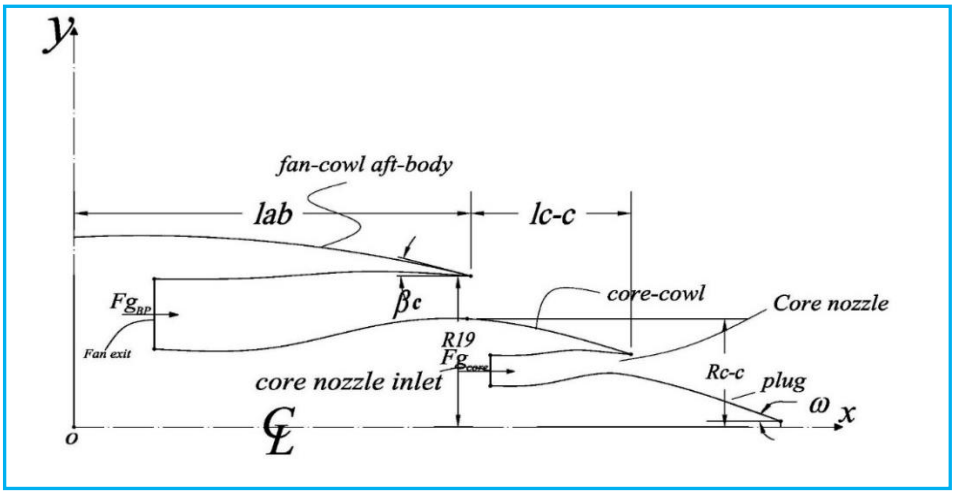


Figure 3 Schematic of the dual-stream nozzle configuration with the geometrical lead parameters.

### 3.2 Numerical domain and boundary conditions

To ensure that the computational boundaries do not affect the aerodynamic characteristic of the nozzle, a domain sensitivity study was conducted. For the single-stream nozzle, four different domain sizes based on the variation of the width (*W)* and height (*H)* have been examined (Figure 4). The baseline domain size was $W = A30D_{max}$ and $H = A10D_{max}$ with $A$ = 1.0. The domain dimensions were changed across $A$ range from 1.0 to 4.0. It was noted that the pressure drag coefficient ( $C_{D\beta}$ ) variation reduced by 0.009% as $A$ increased from 3.0 to 4.0. The domain with a width ($W$) equals to $90D_{max}$ and height ($H$) $30D_{max}$ was chosen for the current investigation.

For the plug nozzle, the domain dimension has been changed axially by A ranging from $A$ = 1.0 to 4.0, starting with a baseline dimension of $W = 25D_{max}$ and $H = 10D_{max}$. The change of the domain size from the third domain ($A$ = 3.0), the fourth domain ($A$=4.0) produces a reduction in the $C_{D\beta}$ by 0.0094 %. The domain of $A$ = 3.0 was chosen to perform the simulations.

For the dual-stream nozzle case, the increase in the domain size showed that $C_d$ variation between domain size of $H = 30D_{max}$ and $W = 90D_{max}$ and $H = 40D_{max}$ and $W = 120D_{max}$ is equal to +0.00007. The thrust coefficient ($C_{fg}$) variation is +0.00009 for dual-stream nozzle configuration. The third domain with $H = 30D_{max}$ and $W = 90D_{max}$ was chosen to carry out the simulations.

The boundary conditions for the current model are the pressure–inlet at the nozzle inlet and the inlet plane of the CFD domain. Uniform total pressure and temperature profiles were set pressure-inlet boundary conditions. The no-slip wall conditions modified the internal walls of the nozzle, the plug, the boat-tail cowl after-body. For the single-stream nozzle, the location of the upstream CFD domain inlet was selected to be $6.0D_{max}$, which is located at the leading edge of the moving part of the experimental nozzle model.

For the plug-nozzle, the distance from the nozzle rim to the CFD domain inlet ($l_{us}$), was selected based on the boundary layer characteristics that are provided by Harrington [14]. The boundary-layer characteristics have the ratio of momentum thickness to the maximum diameter ($\frac{\theta}{Dmax}$) equal to 0.02 at the nozzle rim at $M_\infty = 0.91$. This value is constant across a range of $M_\infty$ from 0.70 to 1.19 [24]. Harrington [14] also found that the boundary velocity profile is similar to a $1/7^{th}$ power law. Thus, the length of the upstream distance ($l_{us}$) from the nozzle rim was calculated based on flat-the plate turbulent boundary layer theory to determine the boundary-layer thickness. This calculation produced an upstream length equals to $3.5D_{max}$. For the dual-stream nozzle, the same boundary conditions were used, Figure 5. However, the slip wall boundary condition was applied to the domain boundaries extended from the location of the engine intake lip (of the full nacelle) to the inlet of the CFD domain, (Figure 5).

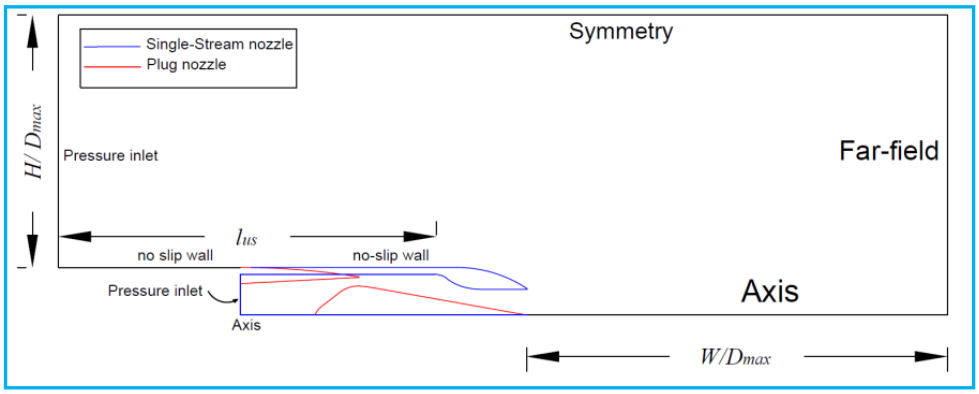


Figure 4 Sketch of the CFD domain for single stream and plug nozzle, showing the employed boundary conditions and the domain geometrical features.

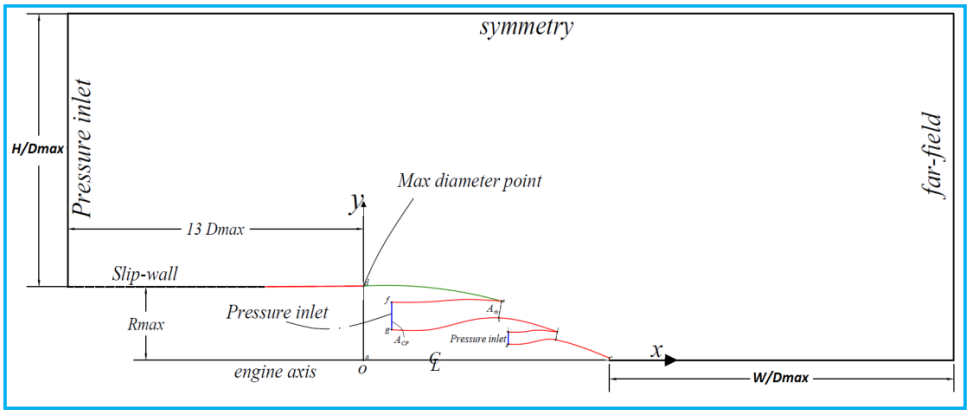


Figure 5 Sketch of the CFD domain for dual-stream nozzle configuration, showing the employed boundary conditions and the domain geometrical features

### 3.3 Meshing Method

A multi-block structured mesh topology was used. The mesh was refined sufficiently in a region where there are significant changes in the flow features, particularly through the exhaust jet region. The boundary layer mesh provided a wall distance ($y^+$) of less than or equals to one. The mesh growth ratio, for the single-stream nozzle, in the radial direction was 1.30 across the boundary layer region and 1.20 for the external domain, whereas for the plug nozzle is 1.27 and 1.30, respectively.

A grid sensitivity study for both configurations was conducted. For the single-stream nozzle, the number of mesh elements was increased from $1.62x10^5$ to $4.0x10^5$ with an average refinement ratio of 1.57, and for the plug nozzle, the number of mesh elements was increased from $2.7x10^5$ to $7.6x10^5$ with average refinement ratio of 1.66. The value of the drag coefficient of the boat-tail was assessed to check their dependence on the number of elements. These meshes were chosen to report the Grid Convergence Index (GCI) [25]. The value of the $GCI_{1,2}$ (between the medium and fine mesh) was 0.001% for the single-stream nozzle and of 0.026% for the plug nozzle. The mesh of the $4.0x10^5$ elements has been chosen to implement the single-stream simulations, and the mesh of $5.0x10^5$ elements has been chosen to implement the plug nozzle simulations.

For the dual-stream nozzle, the number of the mesh elements was increased by refinement ratio of 1.47 from $1.0x10^5$ to $2.3x10^5$. The value of discharge ($C_d$) and thrust coefficient ($C_{fg}$) was assessed to check their dependence on the number of elements. The last three meshes were chosen to report the Grid Convergence Index (GCI). The $GCI_{12}$ for $C_d$ for the by-pass and core nozzle 0.0006% and 0.004%, moreover the $GCI_{12}$ that was calculated based on $C_{fg}$ values is 0.003%. The GCI aspect ratio was found to be is 1.0.

### 3.4 Numerical scheme and boundary conditions

Favre-Averaged Navier-Stokes (FANS) numerical methodology coupled with the k-ω Shear-Stress Transport (SST) turbulence model was employed. The simulations were conducted using a steady state, implicit and density-based solver. The Green-Gauss node-based method was used to compute the flow field gradients. A second-order accurate upwind scheme was employed for the spatial discretization of the flow field. Sutherland's law was utilised for the calculations of dynamic viscosity [21], kinetic theory for the thermal conductivity and temperature-based polynomial correlation to estimate the specific heat [21].

## 4.0 NOZZLE PERFORMANCE CALCULATION METHOD

The nozzle efficiency is represented in the experimental data that are used for the current validation, by the ratio of the thrust-minus-drag (F-D) to the ideal nozzle thrust ($F_i$) [14,18]. Reubush et al., [18] have calculated the F-D term, using an internal three-component strain-gage balance adding to it the internal pressure forces, while Harrington et al., [14] measured the F-D term by using a load cell. In the current CFD calculations, the F-D term was calculated by subtracting the pressure and friction drag components from the actual nozzle gross thrust ($F_g$), (Equation 1). Where $F_g$ represents the momentum flux (or stream thrust)[26] and the pressure thrust at the charging station. The gauge pressure and shear forces were integrated over the walls of the core-cowl, plug, and the nozzle's internal walls. The integration was implemented in the axial direction. The isentropic velocity is calculated using Equation 2. Nozzle efficiency is represented by the $C_{fg}$, (Equation 3). The discharge coefficient ($C_d$) was calculated using Equation 5. The actual mass flow rate was calculated at the nozzle inlet plane ($m_a$). The ideal mass flow rate of the nozzle is evaluated by Equation 6. Where $T_o$ is the total temperature at the nozzle inlet, R is the gas constant, γ is the heat capacity ratio and the subscript (crit) denotes the choked NPR. Furthermore, for the dual-stream nozzle configuration the actual thrust was calculated by adding the by-pass nozzle thrust to core nozzle thrust The thrust coefficient, in this case, was represented by the overall all thrust coefficient ($C_{fgo}$).

$$(F-D) = F_g - \left( \int_{plug+aft-body} (p - p_\infty) d\vec{A} + \int_{plug+aft-body} \tau \, d\vec{A} \right) \quad (1)$$

$$V_s = \sqrt{\frac{2\gamma R T_0}{(\gamma-1)} \left( 1 - \left( \frac{1}{NPR} \right)^{\frac{\gamma-1}{\gamma}} \right)} \quad \ldots(2)$$

$$C_{fg} = \frac{(F-D)}{Fi} \quad \ldots(3)$$

$$Fi = \dot{m_i} V_s \quad \ldots(4)$$

$$C_d = \frac{\dot{m_a}}{\dot{m_i}} \quad \ldots(5)$$

$$(\dot{m})_i = P_0 A_i \left( \frac{1}{NPR_{crit}} \right)^{1/\gamma} \sqrt{\frac{2\gamma}{(\gamma-1)RT_0} \left( 1 - \left( \frac{1}{NPR_{crit}} \right)^{\frac{\gamma-1}{\gamma}} \right)} \quad \ldots(6)$$

# 5.0 RESULTS AND DISCUSSION

## 5.1 Nozzle aerodynamics

### 5.1.1 Single-stream nozzle

The simulations to examine the effect of the fineness ratio and the operational conditions have been conducted using a two-equation turbulence model (SST k-ω). The pressure distribution over the boat-tail of the subsonic free-stream velocity case ($M_\infty$= 0. 8) for the three nozzle configurations shows an agreement with the experimental data through the region of flow expansion over the boat-tail, with pressure coefficient difference ($\Delta Cp$) of -0.016 at $x/l_{bt}$=0.0 at NPR=2.02 for the configuration (1) ($\frac{l_{bt}}{D_{max}}$=0.8, $\beta_c$=17°), (Figure 6). However, an over-prediction of $Cp$ was noted along the separation region extended from at $\frac{x}{l_{bt}} = 0.65$ to $\frac{x}{l_{bt}} = 1.0$, with ($\Delta Cp$) of 0.083 at $\frac{x}{l_{bt}} = 1.0$ for this configurations.

The separation region is distinguished by plateau $Cp$ curve at the region close to the nozzle rim. The curve flattens due to the equalised axial pressure distribution in the separated boundary layer. This behaviour is significantly noticeable for the configuration with a low fineness ratio (configuration (1) ($\frac{l_{bt}}{D_{max}}$ = 0.8, $\beta_c$ = 17°) and configuration (2) ($\frac{l_{bt}}{D_{max}}$ = 1.0, $\beta_c$ = 13.75°). However, the CFD results show that the pressure is still in increase after passing through the separation location indicated by the experimental data. This means that capturing the separation of the flow in the computed data is delayed. This could produce a higher calculated average pressure force over the boat-tail surface than the measured one because the flow will be attached through a larger area of the boat-tail in the separated region. Although the k-ω SST turbulence model was modified using blending function to ensure the use of the k-ω model to compute the boundary-layer characteristics, for the current case, there is a measure of a discrepancy.

As the fineness ratio increases, from $\frac{l_{bt}}{D_{max}}$ = 0.80 to $\frac{l_{bt}}{D_{max}}$ = 1.77, the separation region decreases owing to the reduction in the boat-tail chord angle ($\beta_c$ from 17°-7.8°) and lengthening the boat-tail. This makes the predicted data using the numerical calculations have less deviation from the measured data at high fineness ratio values. This can be seen in configuration (2) ($\frac{l_{bt}}{D_{max}}$ = 1.0, $\beta_c$ = 13.75°) results, where the pressure coefficient difference between the measured and the calculated data is 0.0139% at $x/l_{bt}$= 0.02 and 0.065% at $x/l_{bt}$ = 1.0, these values are lower than the configuration (1) results (Figure 6). Moreover, as the fineness ratio increase to higher levels

(configuration (3) ($\frac{l_{bt}}{D_{max}}$ = 1.77, $\beta_c$ = 7.8 °)) the pressure coefficient difference ($\Delta Cp$) reduces to 0.0430 at *x/l* = 1.0, (Figure 6). The separation almost disappeared for configuration (3) as a result of the reduction in $\beta_c$ so that the flow speed reduced over the convex part of the boat-tail is the minimum, therefore less extreme adverse pressure gradient is expected. This can be seen clearly in Figure 7, where the reversed flow vortex size is in reduction as the value of $\beta_c$ reduces, until it disappeared for configuration (3) ($\frac{l_{bt}}{D_{max}}$ = 1.77, $\beta_c$ = 7.8 °).

The speed of the external flow has an impact on the location of the separation point. By increasing the free stream Mach number, from subsonic speed ($M_\infty$ = 0.4) to transonic ($M_\infty$ = 0.8), the location of the point where the flow separates moves upstream for the same configuration (configuration (2) ($\frac{l_{bt}}{D_{max}}$ = 1.0, $\beta_c$ = 13.75° )), (Figure 8). The separation over the boat tail surface takes place at $\frac{x}{l_{bt}} = 0.8$ when $M_\infty$ = 0.4, whereas at $M_\infty$= 0.8 the separation occurs at $\frac{x}{l_{bt}} \approx 0.65$, (Figure 8). This can be attributed to the increase in the pressure gradient over the boat-tail at $M_\infty$ = 0.8 than the subsonic free stream at the same region from $\frac{x}{l_{bt}} = 0.43$ to $\frac{x}{l_{bt}} = 0.7$ ,(Figure 8).

At supersonic speed, the pressure distribution shows a completely different trend, as there is a continuous pressure drop over the boat-tail surface until the flow pressure reaches to the critical pressure coefficient where the flow shocks. The shock takes place at $\frac{x}{l_{bt}} = 0.65$ and it agrees with the experimental data with pressure coefficient (Cp) of -0.42, (Figure 8). After the shock, the flow separates where the experimental data showed a levelled off pressure distribution. The Mach number contours and the streamlines behaviour show that the size of the separation vortex increases with free-stream Mach number as a sign of an increase of the flow separation region. Moreover, the presence of the normal shock wave (normal to the upcoming flow) separate the flow heavily, produces a large separation region, (Figure 9), and a sudden increase in the pressure.

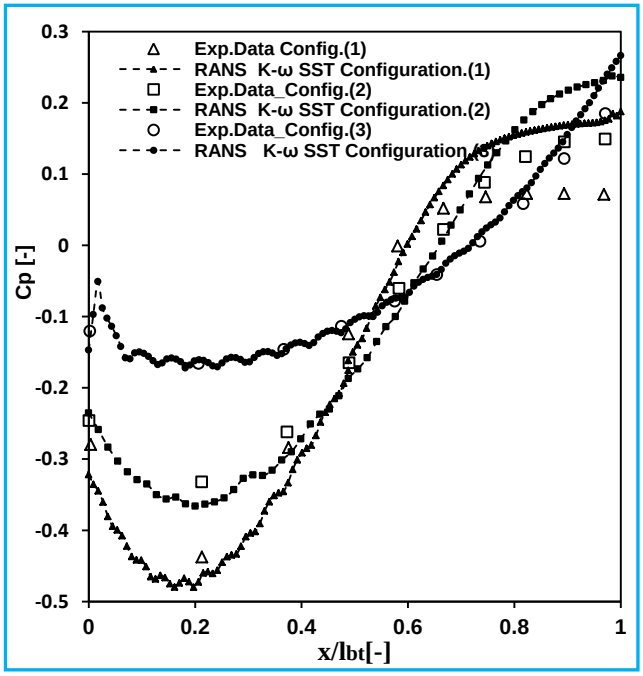


Figure 6 Experimental and CFD pressure coefficient distribution comparison (Cp), over the Boat-tail, between the three configurations of the single -stream nozzle, at the free stream ($M_\infty$) of 0.8 and NPR of 2.02, the CFD Turbulence model is k-ω SST.

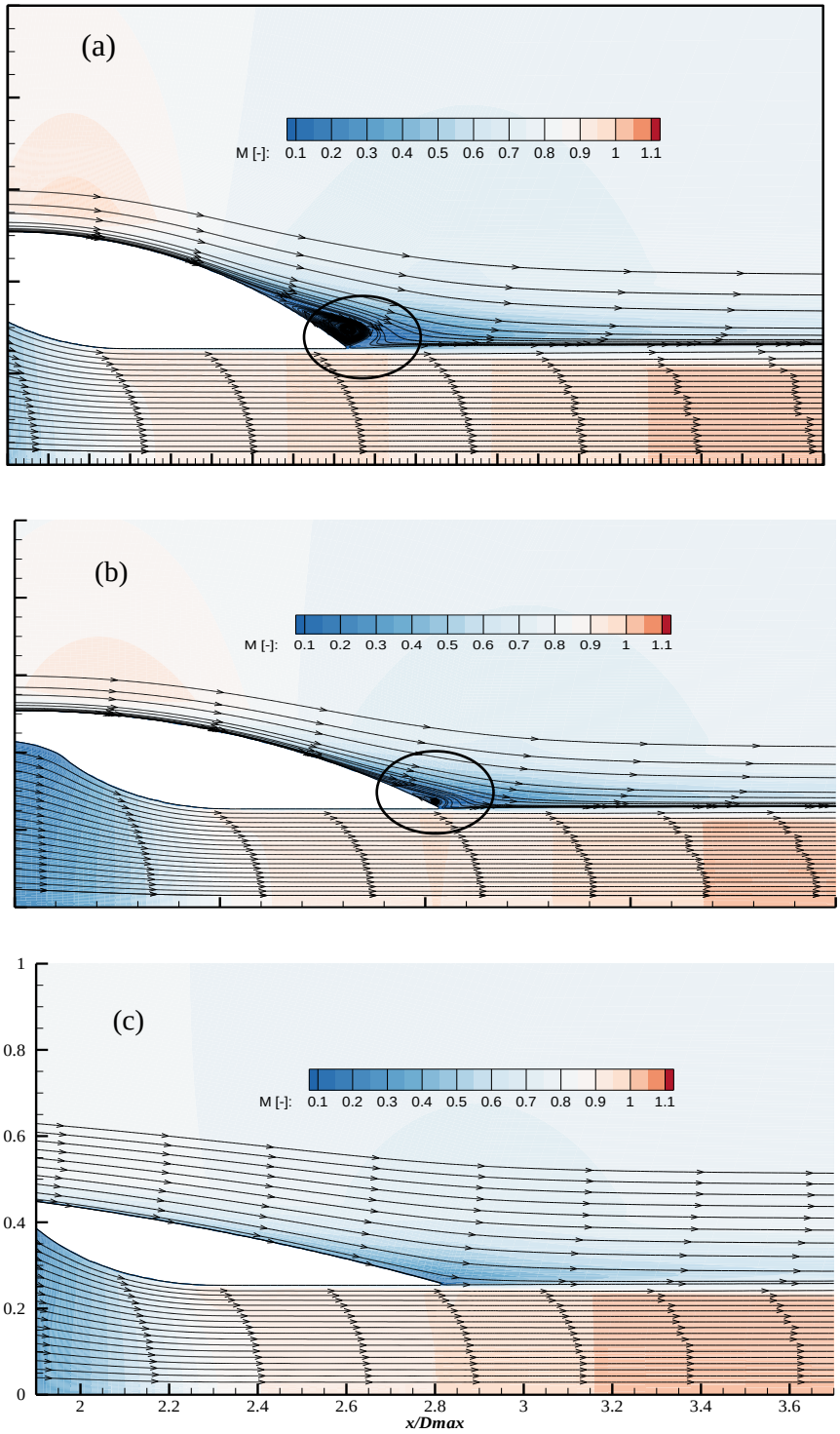


Figure 7 Mach number contour and streamlines distributions around the single stream nozzle comparison between the three configurations, at $M_\infty$ = 0.8 and NPR = 2.02; a) $\frac{l_{bt}}{D_{max}}$ = 0.8, b) $\frac{l_{bt}}{D_{max}}$ = 1.0, c) $\frac{l_{bt}}{D_{max}}$ = 1.77.

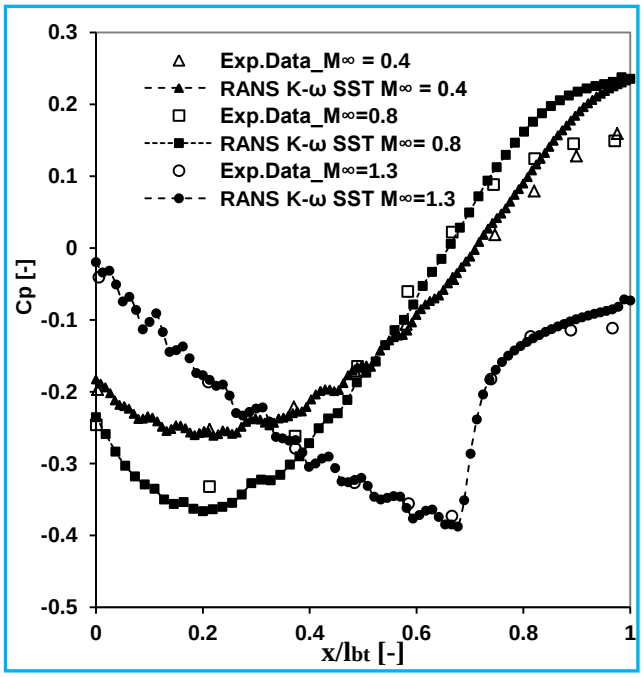


Figure 8 Experimental and CFD pressure coefficient distribution comparison (Cp), over the Boat-tail, between three different free-stream Mach numbers of the single-stream nozzle, at NPR of 2.02, for Configuration (2)($l_{bt}/D_{max}$ =1.0), the CFD Turbulence model is k-ω SST.

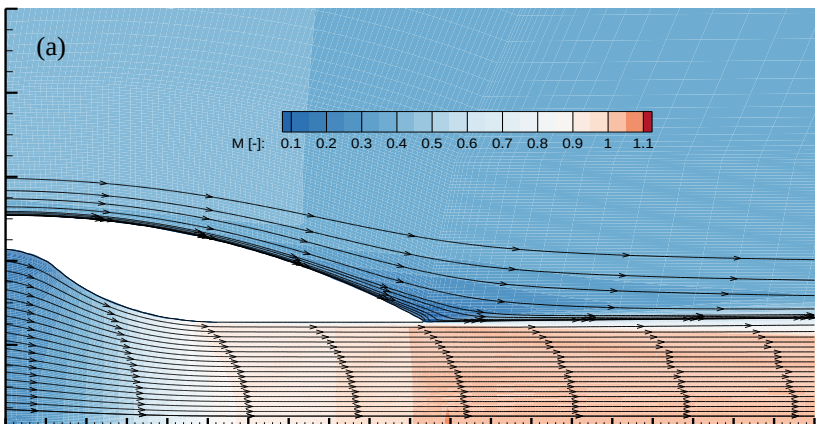

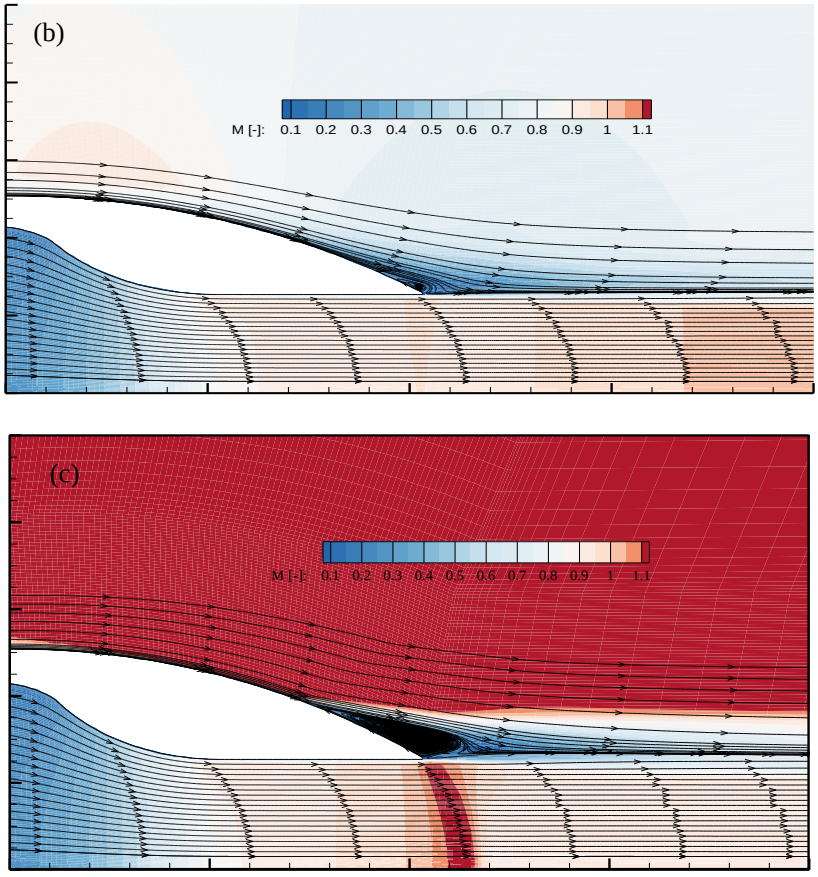


Figure 9 Mach number contour and streamlines distributions around the single stream nozzle comparison between the three Mach numbers ($M_\infty$) =0.4, 0.8 and 1.3 and NPR =2.02, for configuration (2) (($l_{bt}/D_{max}$ =1.0, βc=13.75°)); a) $M_\infty$ = 0.4, b) $M_\infty$ = 0.8, c) $M_\infty$ =1.3.

The performance of different turbulence model was assessed. The single-stream nozzle configurations ($l_{bt}/D_{max}$ = 0.8, $\beta_c$ = 17°) have been used in the validation of the turbulence models. The results show that the RANS k-ω SST model and the realizable k-ε model results are similar in terms of predicting the pressure distribution over the boat-tail with a small deviation between them, across the region between $x/l_{bt}$ = 0.49 to $x/l_{bt}$ = 0.72, (Figure 8). Both of them show a close agreement with the experimental data. The absolute difference of the average pressure coefficient from the experimental pressure coefficient ($\Delta Cp_{ave}$) is 0.050 % for the realizable k-ε model, 0.049 for the RANS k-ω SST, (Figure 10). However, as the flow separates, the RANS k-ω SST match better in terms of the location of the separation point that is indicated by the experimental data. The realizable k-ε model, on the other hand, simulates the separation point at a location further down-stream. This also applies to the SA, skε and RNG kε models, where these models show a downstream movement of the separation point.

Once the flow was separated, an overproduction for the pressure distribution over the boattail surface was overpredicted by all the turbulence model results. The maximum difference in the pressure coefficient ($C_p$) was observed from the sk-ε model with pressure with a difference of ≈ 0.20% at $x/l_{bt}$ = 1.0. The results of the standard k-ω and k-ω SST show better agreement with the measured data from the other models with pressure coefficient difference of 0.10% at $x/l_{bt}$ = 1.0. This was expected as the k-ω model was modified to simulate the flow at low-speed regions.

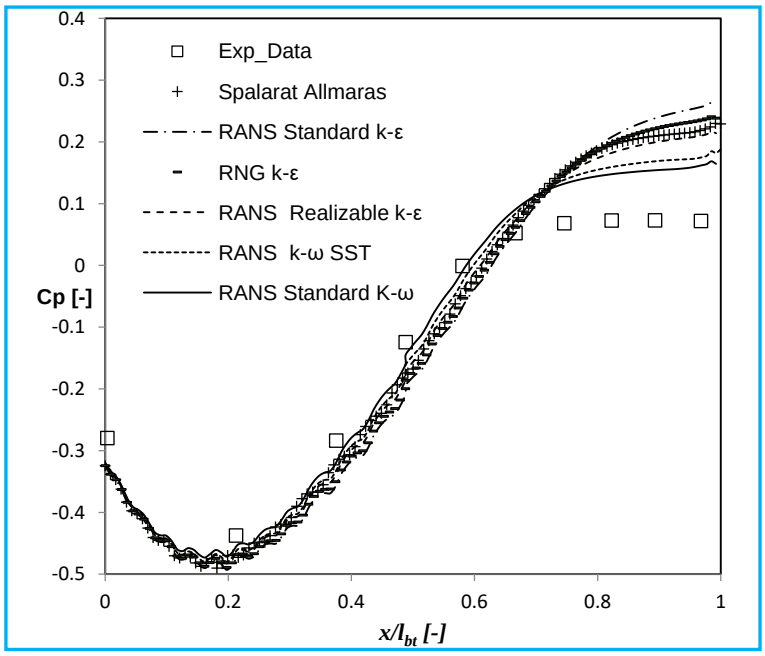


Figure 10 pressure coefficient comparison between different turbulent models for the flow over the single-stream nozzle of Configuration (1) ($\frac{l_{bt}}{D_{max}}$=0.8, $\beta_c$=17° ) , at $M_\infty$ = 0.8 and NPR = 2.02.

### 5.1.2 Plug-nozzle

The aerodynamic results of the plug nozzle are represented by the local static pressure distribution over the plug. These pressure values have been normalised by the nozzle inlet total pressure ($P_7$), to match the available experimental data. The results of the RANS k-ω SST model show that, at transonic Mach number ($M_\infty$=0.91) and NPR of 2.66, the static pressure ratio distribution ($p/P_7$) over the plug surface agrees with the experimental data, (Figure 10). It was found that the absolute average difference of the pressure ratio $\Delta(\frac{p}{P_7})_{ave}$ is 0.00127. At higher NPR (3.71) the numerical model results show disagreement with the experimental data at one data point located at $x/l_{pl}$=0.5, (Figure 11). However, it predicts the location and strength of the other expansion and compression waves over the plug fairly well.

The results showed an increase in the NPR from 2.66 to 3.71 at the same free stream Mach, increases the size of the first expansion region and moves the compression wave location further downstream from $x/l_{pl}$ = 0.19 to $x/l_{pl}$ = 0.25, (Figure 11). Moreover, the increase in the NPR reduces the levels of the pressure over the plug surface, from maximum compression peak of $p/P_7$, = 0.49 at NPR of 2.66 to $p/P_7$ =0.38 at NPR = 3.71. The reduction in the pressure can be attributed to the increase in the jet inclination angle toward the nozzle axis; therefor, the area of the upcoming free stream tube increased. As a result, the pressure over the plug surface increased.

It was noted that increasing the NPR produces a series of weak compression and expansion waves after the compression wave. This was expected, as the increase in the NPR, strong under-expansion nozzle behaviour is captured, this causes more expansion process to take place after the nozzle exit. This is not applicable with NPR of 2.66, as the first expansion was enough to bring the exit nozzle static pressure close to the free stream pressure, (Figure 12).

Most of the turbulence models show the same level of capability for capturing the shock wave's strength and the location at the nozzle exit at NPR 2.66 and $M_\infty$= 0.91, (Figure 13). Downstream of the compression wave, the flow exhibits a weak expansion and compression waves, and the models predicted the pressure distribution with only a small deviation from the experimental data.

At NPR = 3.12 and $M_\infty$ = 0.60, the k-ε family turbulence models showed completely different behaviour from the other models, (Figure 14). These turbulence model results over-predicted the compression wave strength at $x/l_{plug}$ = 0.2 and then developed four shock cells which are in agreement with the experimental data, but the location of the waves is predicted to be further downstream than was indicated by the experimental data. Apart from the first expansion wave, the k-ω model results did not predict the presence of four shock cells over the plug surface under this operational condition, (Figure 14).

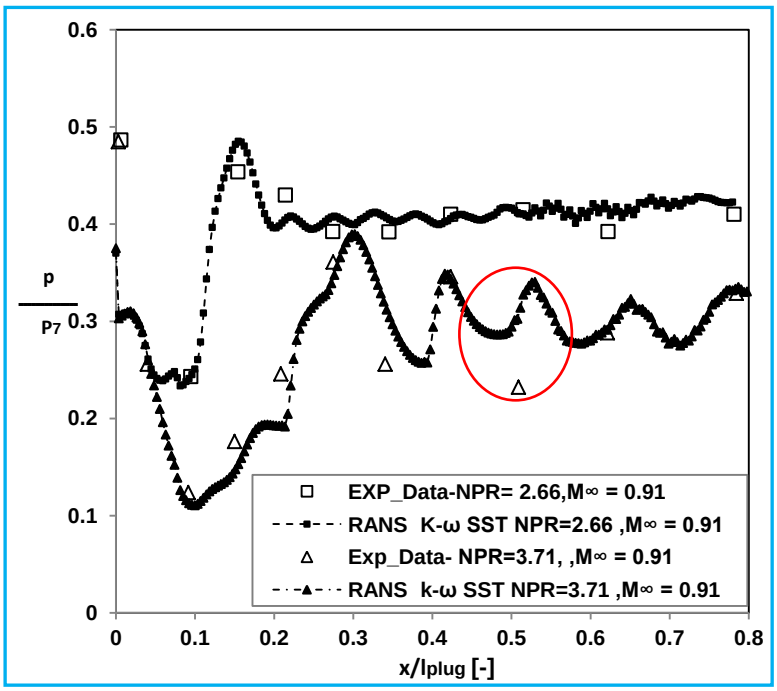


Figure 11 Comparison of plug surface pressure distribution between the CFD turbulence models and the experimental data at free stream $M_\infty$ No. of 0.91 and two NPR 2.66 and 3.71.

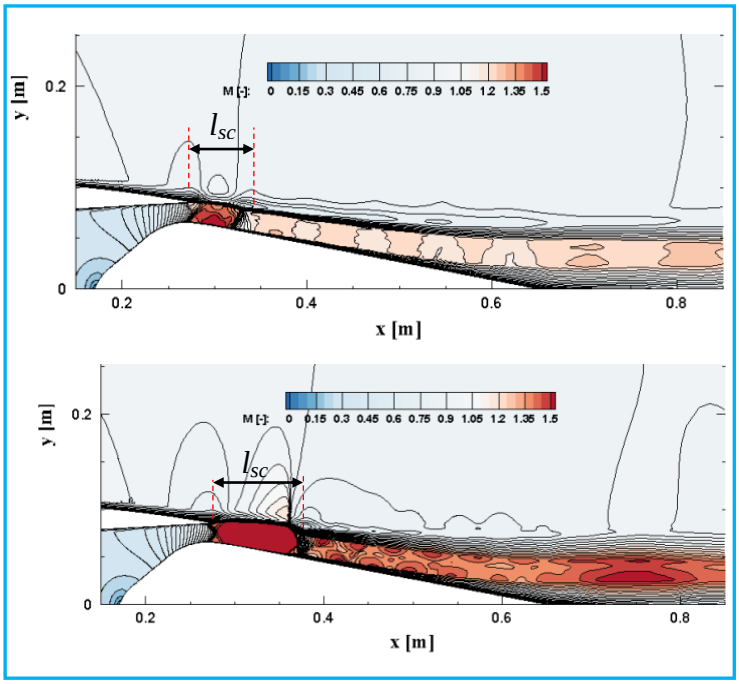


Figure 12 Mach number contour around the plug nozzle at two different operation conditions, (a) at NPR = 2.66 and $M_\infty$= 0.91, (b) at NPR = 3.71 and $M_\infty$ = 0.91.

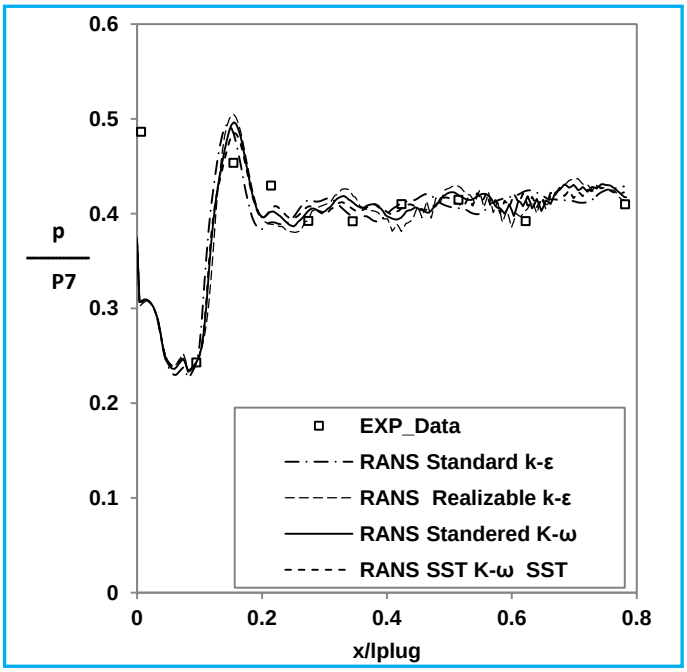


Figure 13 plug surface pressure distribution over plug comparison between the CFD turbulence models and the experimental data at free stream number ($M_\infty$) of 0.91 and NPR of 2.66.

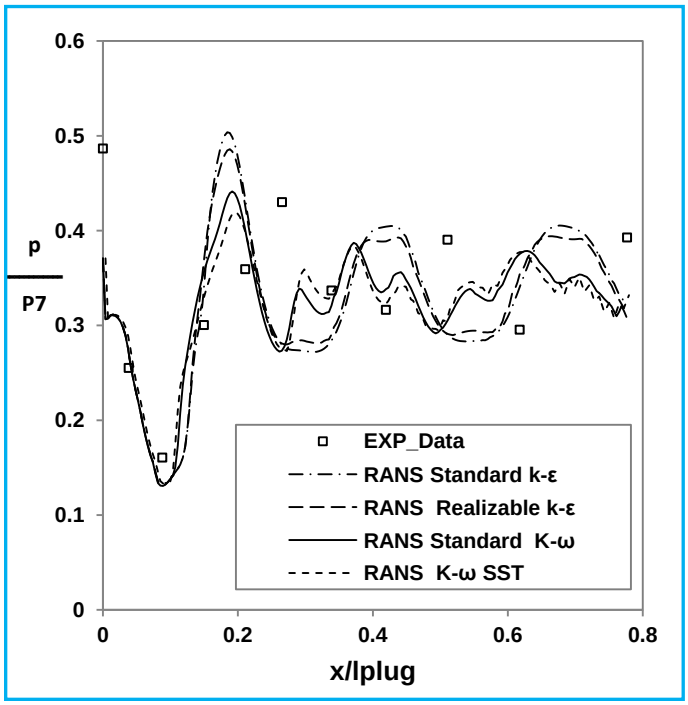


Figure 14 plug surface pressure distribution over plug comparison between the CFD turbulence models and the experimental data at free stream number ($M_\infty$) of 0.6 and NPR of 3.71.

## 5.2 Nozzles performance evaluation

### 5.2.1 Single stream nozzle

The NPR range was extended from 1.83 to 3.88 for the single-stream nozzle to be comparable with the measured data. The results of the k-ω SST model showed that, for the single-stream nozzle, the computed performance data were lower than the experimental data by ≈ 3.29% at NPR = 1.83 and by -0.84% at NPR = 3.88, (Figure 15).

The realizable k-ε result for the single-stream nozzle predicted the nozzle performance better than the SA and k-ω SST model data (Figure 15).

### 5.2.2 Plug nozzle

The NPR range was extended from 2.60 to 6.33. The numerical results for the plug nozzle predicted the nozzle efficiency with percentage difference from the measured data of -1.05% at NPR = 2.64 and across a range from -0.46% to -0.68% between NPR = 3.14 to 5.3. The results deviate equally from the predicted nozzle efficiency of Malecki et al., [13], (Figure 16). The turbulence model validation showed that k-ω SST model data showed the best prediction of the nozzle performance.

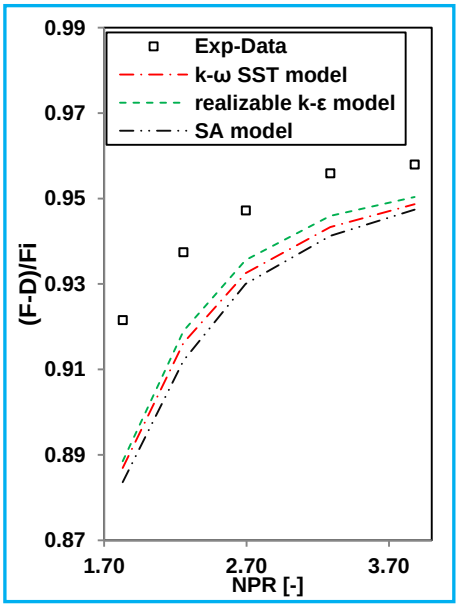


Figure 15 Comparison of the CFD and the experimental single stream nozzle efficiency (configuration 1) at $M_\infty = 0.90$ as a function of NPR, for the chosen turbulence model.

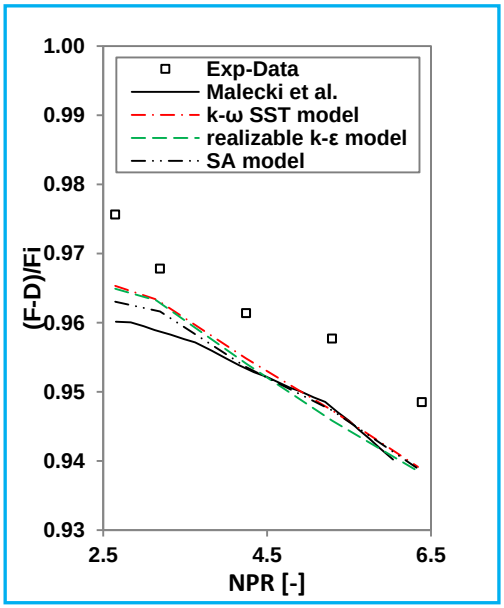


Figure 16 Comparison between the CFD and experimental plug nozzle efficiency at $M_\infty = 0.91$ with NPR, for the chosen turbulence model.

## 5.3 Dual-stream nozzle

### 5.3.1 Overall nozzle performance

The results of the overall nozzle performance are represented by $C_{fg}$ (Figure 17). The results showed an increase in the performance with CNPR and plug-half angle (ω). This increase started from NPR 1.4 to 2.0; afterwards, the performance of the nozzle configuration with large ω (from 15º to 20º) decreases. This decrease can be attributed to the separation of the flow over the plug surface as a result of the increase in ω and the flow velocity with the CNPR, and the reduction in the pressure over the plug surface, Figure 17. The increase in the overall performance of the nozzle is attributed to the increase in the pressure forces intensity over the plug surface with the CNPR (Figure 18). The increase in ω will pull down the stream tube of the bypass nozzle jet, causing an enlargement in the stream tube area and hence the pressure. With further increase in the CNPR and ω, the performance degraded. As a result of that, the flow separation over the plug surface as a result of the increase in the CNPR and ω.

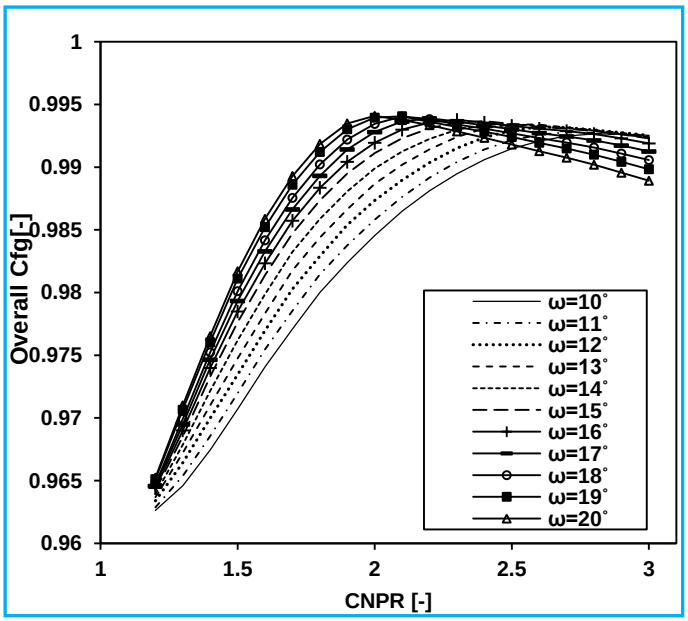


Figure 17 Overall dual-stream nozzle gross thrust coefficient as a function of the CNPR for the chosen plug half-angle, for nozzle configuration at FNPR = 2.40.

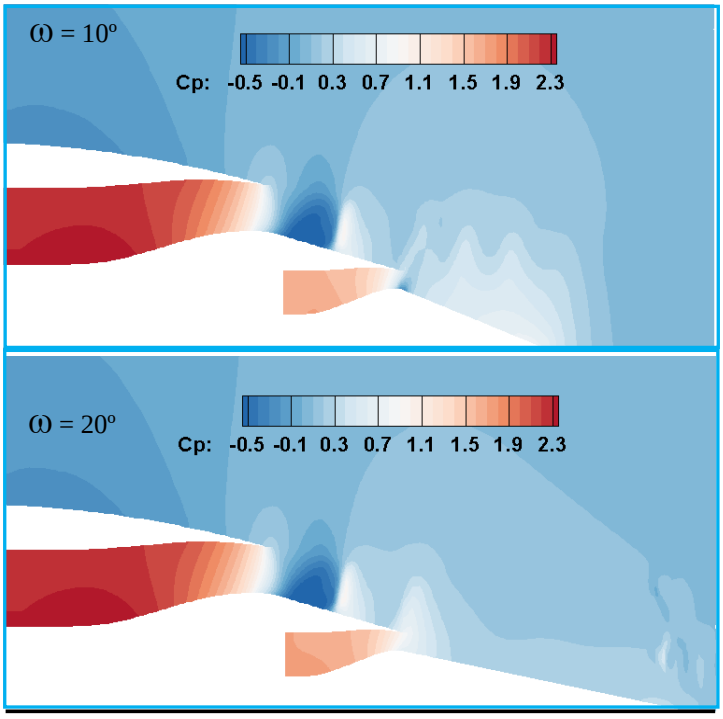


Figure 18 Pressure coefficient contour (Cp) around the exhaust system for a configuration (a) ω = 10º, (b) ω = 20º.

### 5.3.2 Core nozzle performance

The results showed that the core nozzle discharge coefficient is extremely affected by the bypass nozzle flow. When the FNPR = 1.0, the bypass nozzle has no impact on the core nozzle, (Figure 19), in which an insignificant variation in $C_d$ was observed. However, at high FNPR, the bypass stream tube hugely affects the core nozzle $C_d$, figures from Figure 20 to Figure 22. This is attributed to the increase in the static pressure levels that is surrounding the core nozzle with the presence of the fan nozzle jet. Furthermore, the variation of the plug half-angle (ω) is also affecting the performance of the core nozzle. However, ω variation effect is very small when there is no fan flow and increases with the increase in the FNPR. It can be seen that the core

nozzle $C_d$ increases with the growth in ω, particularly across the region of the core nozzle pressure ratio (CNPR) 1.4 to 2.0, Figure 21. It was also noted that the choking CNPR decreased with the increase in ω.

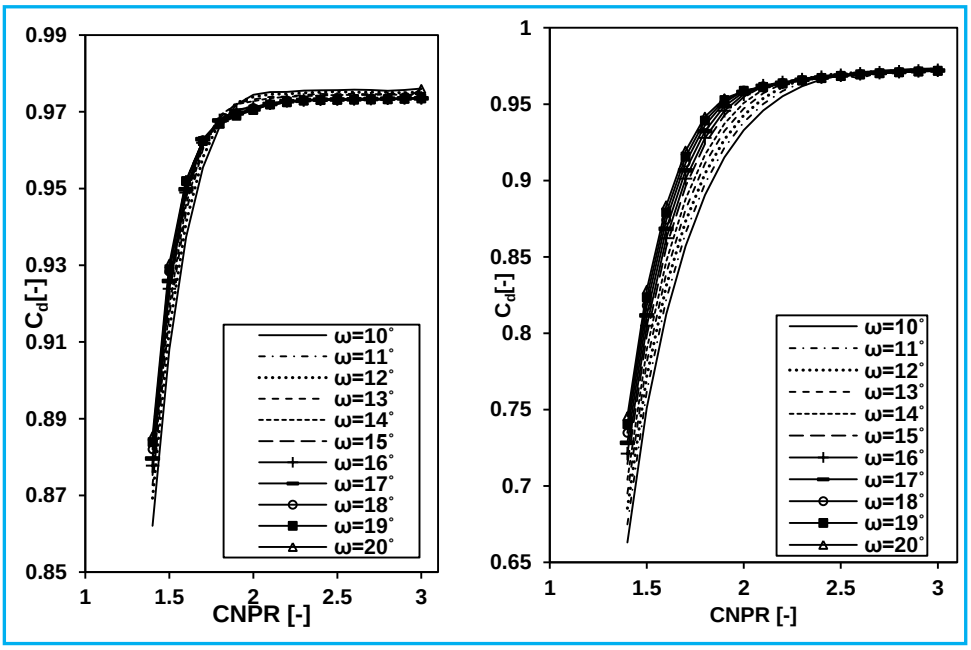


Figure 19 Discharge coefficient of the core nozzle, as a function of CNPR for the chosen β; for nozzle configuration of CR = 1.50 at FNPR = 1.0.




Figure 20 Discharge coefficient of the core nozzle, as a function of CNPR for the chosen β; for nozzle configuration of CR = 1.50 at FNPR = 2. 0.

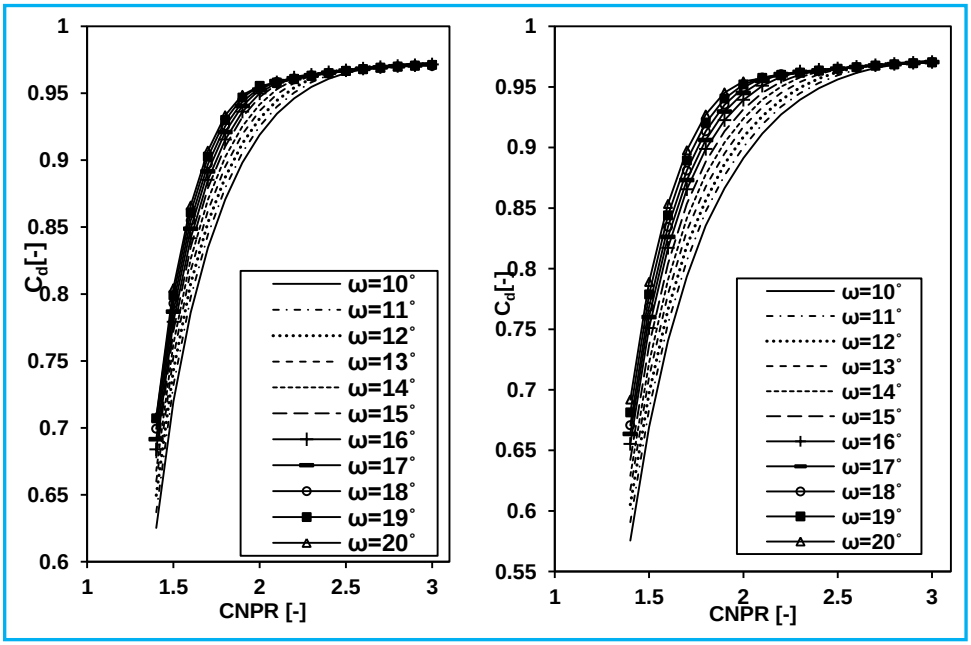


Figure 21 Discharge coefficient of the core nozzle, as a function of CNPR for the chosen ω, at FNPR = 2.20.




Figure 22 Discharge coefficient of the core nozzle, as a function of CNPR for the chosen ω, at FNPR = 2.40.

At FNPR = 1.0, the thrust coefficient of the core nozzle showed an increase at small boat tail levels (ω) and decreases at high CNPR and ω, (Figure 22 a). This behaviour is contrasted when the flow of the bypass nozzle presented (Figure 22 b-d). The thrust coefficient ($C_{fg}$) increase noticeably with ω across CNPR range from 1.2 to a maximum value of $C_{fg}$ at CNPR ($CNPR_{max}$) of 1.90, Figure 23. The value of $CNPR_{max}$ at which $C_{fg}$ reaches to its maximum value is changeable with ω. When the plug half-angle (ω)

increases, the value of $CNPR_{max}$ decrease. It can be concluded that the combined impact of the aerodynamic and the geometric parameters on the nozzle performance is considerable, and it needs to be investigated in detail.

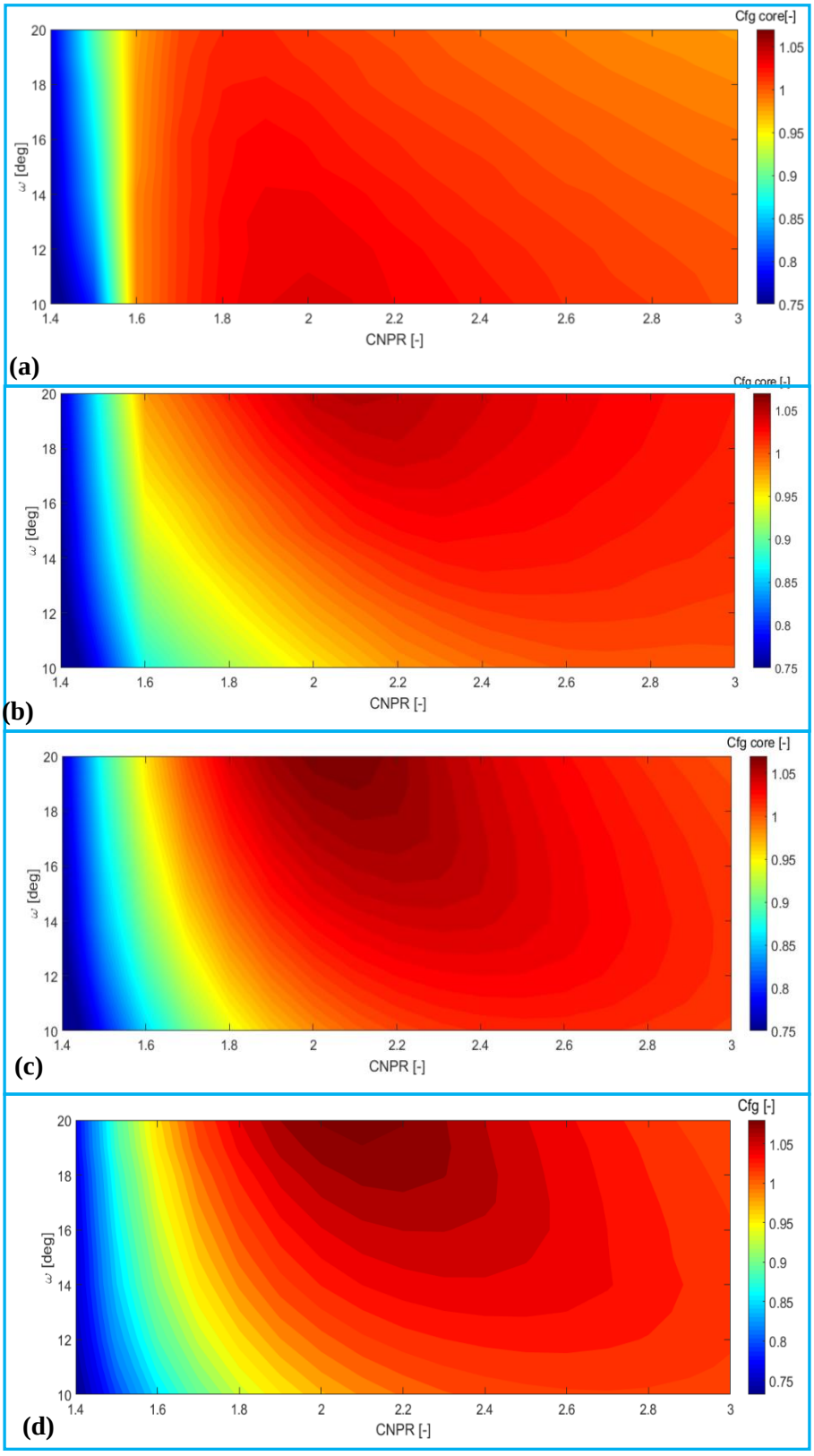


Figure 23 Core nozzle gross thrust coefficient ($C_{fg}$) as a function of the CNPR for the chosen plug half-angle at; (a) FNPR = 1.0, (b) FNPR = 2.0, (c) FNPR = 2.2, (d) FNPR = 2.4.

# 6.0 CONCLUSION

Nozzle computational models were developed to assess the exhaust system performance. A set of previous experimental data were used to assess the module performance in predicting the nozzle aerodynamic characteristic correctly. A comparison between the calculated and the measured aerodynamic performance for two types of propelling nozzles was presented. Three single-stream nozzle configurations were examined with a different fineness ratio of ($\frac{l_{bt}}{D_{max}}$ = 0.8, 1.0 and 1.77). The simulations were conducted at different operating conditions. It is concluded that:

1- The pressure coefficient distribution over the boat-tail of the single-stream agrees with the measured data through the attached flow region, as the pressure coefficient difference is -0.016 at *x/l* = 0.0, at $M_\infty$ = 0.4 and NPR = 2.02 for the configuration (1) ($\frac{l_{bt}}{D_{max}}$ = 0.8, $\beta_c$ = 17°). The numerical model over-predicts pressure distribution over the boat tail at the separation region with ($\Delta Cp$) of 0.083 at *x/l* =1.0.

2- The numerical model shows a quantitative and qualitative agreement with the experimental data of the flow over the plug surface. However, it gives better results at relatively low NPR (less than 3.12).

3- The application of RANS k-ω SST turbulence model is preferred in aero-engine exhaust system simulations as it shows the best agreement with the experimental data than the other models.

4- The nozzle efficiencies that have been derived from the CFD calculations have lower levels in comparison with the experimental data for both nozzle types, with a maximum difference of single-stream nozzle efficiency ≈ 3.29% at NPR = 1.83 and by 0.84% at NPR = 3.88 and for the plug nozzle with -1.05% at NPR 2.64 and across a range from -0.46% to -0.68% between NPR =3.14 to 5.3.

5- The fan nozzle pressure ratio (FNPR) and the plug half-angle (ω) has a noticeable impact on the overall and core nozzle performance.

6- Both the geometrical and aerodynamic parameters have a noticeable effect on the propelling nozzle performance, and they should be examined in detail even from the preliminary design phase.

# REFERENCES

[1] D.J. AND W.A.F. LENNARD, Performance Improvement Features of General Electric Turbofan Engines, ASME 82-GT-270, in: Am. Socity Mech. Eng., ASME 82-GT-270, New York, 1982.

[2] H. ZIMMERMANN, K. AND KATHEDER, A. JULA, A numerical investigation into the nozzle flow of high by-pass turbofans, in: Int. Gas Turbine Aeroengine Congr. Expo., ASME 92-GT-10, Cologne, Germany, 1992: pp. 1–11.

[3] Y. ZHANG, H. CHEN, M. ZHANG, M. ZHANG, Z. LI, S. FU, "Performance Prediction of Conical Nozzle Using Navier–Stokes Computation", *Journal of Propulsion and Power*. 31 (2015) 192–203. doi:10.2514/1.B35164.

[4] N.G. SPOTTS, S. GUZIK, X. GAO, A CFD Analysis of Compressible Flow through Convergent-Conical Nozzles, in: 49th AIAA/ASME/SAE/ASEE Jt. Propuls. Conf., American Institute of Aeronautics and Astronautics, AIAA 2013-3734, CA, 2013. http://dx.doi.org/10.2514/6.2013-3734.

[5] V.F. DIPPOLD, Computational simulations of convergent nozzles, Technical Report, NASA Glenn Research Center, NASA/TM-2014-218329; E-18926;

GRC-E-DAA-TN14457, 2014.

[6] D.J. LAHTI, D.A. DIETRICH, N.O. STOCKMAN, G.K. FAUST, Application of Computational Methods to the Design of Large Turbofan Engine Nacelles, in: AlAA 22nd Aerosp. Sci. Meet., AlAA 84-0121, Reno, Nevada, 1984: pp. 1–12.

[7] R. MALECKI, W. LORD, A 2D Duct / Nozzle Navier-Stokes Analysis System for Use By Designers, in: 31st AIAA/ASME/SAE/ASEE Jt. Propuls. Conf. Exhib., AIAA 95-2624, San Diego, CA, 1995: pp. 1–19.

[8] H. ZIMMERMANN, R. GUMUCIO, K. KATHEDER, A. JULA, T.M. GMBH, CFD Study of Nozzle Configurations for Ultra High Bypass Engines, in: Int. Gas Turbine Aeroengine Congr. Expo., ASME93-GT-389, Cincinnati, Ohio, 1993: pp. 1–14. doi:10.1115/93-GT-389.

[9] A. AL-AKAM, T. NIKOLAIDIS, D.G. MACMANUS, "Computational fluid dynamics-based approach for low-order models of propelling nozzle performance", 0 (2019) 1–16. doi:10.1177/0954410019831852.

[10] K. PEERY, C. FORESTER, Numerical simulation of multi-stream nozzle flows, in: 12th Fluid Plasma Dyn. Conf., AIAA, Williamsburg, Virginia, 1979. doi:10.2514/6.1979-1549.

[11] Y. ZHANG, H. CHEN, M. ZHANG, M. ZHANG, Z. LI, S. FU, "Performance Prediction of Conical Nozzle Using Navier–Stokes Computation", *Propulsion and Power Research*. (2014) 1–12. doi:10.2514/1.B35164.

[12] L.J.H. AND R.E. PONSONBY, Applications of CFD technology to the design of aircraft propulsion systems, in: ICAS, 1990.

[13] R. MALECKI, W. LORD, Aerodynamic performance of exhaust nozzles derived from CFD simulation, in: 31st AIAA/ASME/SAE/ASEE Jt. Propuls. Conf. Exhib., AIAA 95-2623, San Diego, CA, 1995: pp. 1–17.

[14] D.E. HARRINGTON, Performance of Convergent and Plug Nozzles at Mach Numbers from 0 to 1.97, NASA Technical Memorandum-NASA TM X-2112, 1970.

[15] N. SPOTTS, S. GUZIK, "A CFD analysis of compressible ow through convergent-conical nozzles", (n.d.) 1–7.

[16] K.L. MIKKELSEN, D.J. MYREN, D.G. DAHL, M. CHRISTIANSEN, Initial Subscale Performance Measurements of the AIAA Dual Separate Flow Reference (DSFR) Nozzle, in: 51st AIAA/SAE/ASEE Jt. Propuls. Conf., AIAA 2015-3883, Orlando,USA, 2015: pp. 1–30. doi:10.2514/6.2015-3883.

[17] K.S. ABDOL-HAMID, K. UENISHI, B.D. KEITH, J.R. CARLSON, "Commercial turbofan engine exhaust nozzle flow analyses", *Journal of Propulsion and Power*. 9 (1993) 431–436. doi:10.2514/3.23639.

[18] J.F. REUBUSH, D. E, RUNCKEL, Effect of Fineness Ratio on Boattail Drag of Circular-Arc Afterbodies having Closure Ratios of 0.50 with Jet Exhaust at Mach Numbers up to 1.30, NASA Technical Note, TN-7192, 1973.

[19] P. SPALART, S. ALLMARAS, A one-equation turbulence model for aerodynamic flows, in: 30th Aerosp. Sci. Meet. Exhib., American Institute of Aeronautics and Astronautics, 1992. doi:doi:10.2514/6.1992-439.

[20] B. E. LAUNDER AND D. B. SPALDING, Lectures in Mathematical Models of Turbulence, . Academic Press, London, England, 1972.

[21] ANSYS INC., "ANSYS Fluent Theory Guide 14.0, November,2013", (2013).

[22] W.L. MACMILLAN, Development of a modular-type computer program for the

calculation of gas turbine off-design performance, PhD Thesis, Cranfield University,UK, 1974.

[23] B. KULFAN, J. BUSSOLETTI, “Fundamental” parametric geometry representations for aircraft component shapes, in: 11th AIAA/ISSMO Multidiscip. Anal. Optim. Conf., AIAA-2006-6948, Seattle, Washington, 2006: pp. 547–591. doi:10.2514/6.2006-6948.

[24] D.E. HARRINGTON, "Jet effects on boattail pressure drag of isolated ejector nozzles at mach numbers from 0.60 to 1.47", *NASA TECHNICAL MEMORANDUM (TM X-1785)*. (1969).

[25] P.J. ROACHE, "Quantification of uncertainty in computational fluid dynamics", *Annual Review of Fluid Mechanics*. 29 (1997) 123–160. doi:10.1146/annurev.fluid.29.1.123.

[26] J.R. DEBONIS, Gas Turbine Engines: Nozzles, in: Encycl. Aerosp. Eng., John Wiley & Sons, Ltd, 2010. doi:10.1002/9780470686652.eae096.

2019-12-31

# A numerical model for predicting the aerodynamic characteristics of propelling nozzles

Al-Akam, Aws A.

International Society for Air Breathing Engines